Turning Noise into Data: Characterization of the Van Allen Radiation Belt Using SDO Spikes Data

Spiridon Kasapis[1,2], Barbara J. Thompson[1], Juan V. Rodriguez[3,4], Raphael Attie[1,5], Gonzalo Cucho-Padin[6,7], Daniel da Silva[1,8,9], Meng Jin[10], William D. Pesnell[1]

[1]Solar Physics Laboratory, NASA Goddard Space Flight Center, Greenbelt, MD, USA
[2]Department of Climate and Space Sciences and Engineering, University of Michigan Ann Arbor, MI, USA
[3]Cooperative Institute for Research in Environmental Sciences, University of Colorado Boulder, CO, USA
[4]NOAA National Centers for Environmental Information, Boulder, CO, USA
[5]Physics and Astronomy Department, George Mason University, Fairfax, VA, USA
[6]Department of Physics, Catholic University of America, Washington, DC, USA
[7]Space Weather Laboratory, NASA Goddard Space Flight Center, Greenbelt, MD, USA
[8]Goddard Planetary Heliophysics Institute, University of Maryland Baltimore County, Baltimore, MD, USA
[9]Laboratory for Atmospheric and Space Physics, University of Colorado Boulder, CO, USA
[10]Lockheed Martin Solar and Astrophysics Laboratory, Palo Alto, CA, USA

Key Points:

- More than 3 trillion "spiked pixels" attributed to magnetospheric particle impacts have been removed from the SDO/AIA images so far.
- The SDO spike rate was compared to particle measurements from GOES-14 during close orbital conjunctions occurring twice daily over 27 months.
- The high correlation between AIA spikes and GOES-14 electron fluxes indicates that AIA spikes could be a proxy for radiation belt electron fluxes.

Corresponding author: Spiridon Kasapis, skasapis@umich.edu

Abstract

The Solar Dynamics Observatory (SDO) is a solar mission in an inclined geosynchronous orbit. Since commissioning, images acquired by Atmospheric Imaging Assembly (AIA) instrument on-board the SDO have frequently displayed "spikes", pixel regions yielding extreme number of digital counts. These are theorized to occur from energetic electron collisions with the instrument detector system. These spikes are regularly removed from AIA Level 1.0 images to produce clean and reliable data. A study of historical data has found over 100 trillion spikes in the past decade. This project correlates spike detection frequency with radiation environment parameters in order to generate an augmented data product from SDO. We conduct a correlation study between SDO/AIA data and radiation belt activity within the SDO's orbit. By extracting radiation "spike" data from the SDO/AIA images, we produce a comprehensive data product which is correlated not only with geomagnetic parameters such as Kp, Ap and Sym-H but also with the electron and proton fluxes measured by the GOES-14 satellite. As a result, we find that AIA spikes are highly correlated with the GOES-14 electrons detected by the MAGED and EPEAD instruments at the equator (where the two satellites meet) with Spearman's Correlation values of $\rho = 0.73$ and $\rho = 0.53$ respectively, while a weaker correlation of $\rho = 0.47$ is shown with MAGPD protons for the two year period where both missions returned data uninterruptedly. This correlation proves that the SDO spike data can be proven useful for characterizing the Van Allen radiation belt, especially at areas where other satellites cannot.

Plain Language Summary

The Solar Dynamics Observatory (SDO) is a NASA mission that has been observing the Sun since 2010. One instrument aboard SDO is the Atmospheric Imaging Assembly (AIA) which acquires pictures of the Sun in seven extreme ultraviolet (EUV) and two ultraviolet (UV) channels. The AIA detector is designed to capture solar photons of different wavelengths to create images. However, SDO is located in a geosynchronous orbit, which passes through regions of the outer radiation belt. Energetic particles that impact the detector result in brightened pixels in the SDO images. An algorithm removes and records these unusual pixels in every AIA image. Although these pixels are considered noise, in this research we use them to infer the particle density along SDO's orbit. This paper proves that the fluctuation of the number of noisy pixels in AIA's images best matches the fluctuation of the electron readings from the nearby GOES-14 weather satellite. This research shows that these noisy pixels can be turned to a data product useful for characterizing the Van Allen radiation belt.

1 Introduction

Sometimes the proverb "one man's trash is another man's treasure" is also apt in science, as that which is considered noise in one scientific enquiry might be found to be insightful data in another. This has lately been observed in the field of heliophysics.

Early after its launch, the Solar Terrestrial Relations Observatory (STEREO) mission team observed that an unusually high number of spacecraft-related "debris" were being detected by its coronographic instruments (SECCHI suite) compared to other previously flown similar detectors. When St Cyr et al. (2009) compared the SECCHI "debris storms" with S/WAVES, they found that almost all are coincident with the most intense transient emissions observed by the radio and plasma waves instrument. They concluded that the debris came from the spacecraft thermal blanketing caused by impacts of large interplanetary dust grain storms that are detected by S/WAVES. Based on this debris-storm correlation, proxy measurements for interplanetary dust distributions could be obtained.

Using the Solar and Heliospheric Observatory (SOHO) data, Didkovsky et al. (2006) created a tool to indirectly measure proton flux which was based on the energy deposited by protons in 128 × 128 pixel Extreme Ultraviolet Imaging Telescope (EIT) charge-coupled device (CCD) areas outside the solar disk images. This tool was tested by comparing Solar Energetic Particles (SEP) flux temporal profiles extracted from the EIT CCD frames and downloaded from the GOES database for a number of early 2000s events. The SEP flux temporal profiles and the relatively narrow energy ranges between 45 and 440 MeV EIT proton spectra reported in their work correlates well with the GOES profiles. SOHO is at the Sun-Earth first Lagrange point (L1).

Carlton et al. (2018) developed a quantitative technique which using the Galileo spacecraft solid-state imaging (SSI) instrument helps characterize the high-energy electron Jovian environment. In his work he suggests that the approach of using Galileo images backgrounds can be applied to other sets of imaging data (star trackers) in energetic electron environments, such as those found in Geostationary Earth Orbit (GEO). A similar approach is followed in this paper for indirectly inferring electron fluxes within the Van Allen outer radiation belt. Named after James Van Allen who first confirmed its existence using data from Explorer 1, the Van Allen radiation belt was one of the first discoveries of the space age (W. Li & Hudson, 2019). A number of missions (even early ones such as Explorer 3 and 4, Pioneer 3, and Luna 1) have been equipped with instruments which are geared towards mapping the radiation belts, the most representative one being the Van Allen Probes (Kurth et al., 2015).

To get a full picture of the Van Allen radiation belts, satellites that orbit the Earth in unique ways are necessary. A good example, is the Solar Anomalous and Magnetospheric Particle Explorer (SAMPEX), which using its low-altitude polar orbit, has provided a unique long-term global picture of the radiation belts since its launch in 1992 (X. Li et al., 2001). Launched in 1966, the Applications Technology Satellite 1 (ATS-1) was the first to observe charged particle fluxes in geosynchronous orbit (Lanzerotti et al., 1967; Lezniak et al., 1968; G. Paulikas & Blake, 1979). NOAA has monitored solar-origin and radiation belt particles in GEO since 1975 with the long series of Geostationary Operational Environmental Satellites (GOES). In this paper we undertake the challenge of helping this characterization effort using data from the Solar Dynamics Observatory (SDO), a satellite that was not deployed to study the Van Allen radiation belts nor does it carry instruments geared towards such a task. By showing that SDO's spike data (otherwise treated as noise) correlate well with the radiation belt electron flux readings of GOES-14, we prove that in the future it can be used by the space science community as a data product useful for real-time characterization of the radiation belts.

2 SDO Satellite and Orbit

The SDO spacecraft was developed at NASA's Goddard Space Flight Center and launched on 11 February 2010 from the Cape Canaveral Space Force Station as the first flagship mission of NASA's Living With a Star (LWS) program. Although its primary mission was planned to last five years (2015), SDO is expected to remain operational until 2030. Its primary goal is to understand those solar variations that influence life on Earth and humanity's technological systems, aiming towards developing predictive capabilities of the solar activity. Insights gained from SDO investigations aim on giving the heliophysics community a better understanding of how the Sun's magnetic field is generated and structured along with how through solar wind, energetic particles and variations in the solar irradiance, it affects the heliosphere and geospace (Pesnell et al., 2011).

To do the above, other than its two solar arrays and two high-gain antennas, SDO is equipped with three instruments as seen in Figure 1: a) the Extreme Ultraviolet Variability Experiment (EVE Woods et al. (2010)), b) the Helioseismic and Magnetic Imager (HMI, Scherrer et al. (2012)) and c) the Atmospheric Imaging Assembly (AIA, Lemen

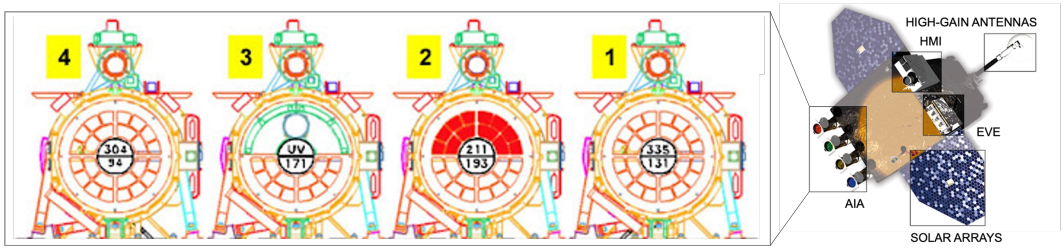

Figure 1: Artist's impression of the SDO Satellite with its High-Gain Antennas, Solar Arrays and three scientific instruments: HMI, EVE and AIA (used in this research). The diagram on the left presents the layout of the wavelength channels or band passes in each of the four AIA telescopes (Lemen et al., 2011; Pesnell et al., 2011)

.

et al. (2011)). The instruments were built in partnership with the University of Colorado Boulder's Laboratory for Atmospheric and Space Physics (LASP), Stanford University Hansen Experimental Physics Laboratory (HEPL) and Lockheed Martin Solar and Astrophysics Laboratory (LMSAL) respectively.

This research uses meta-data associated with AIA's high-resolution full-disk images of the corona and solar transition region, taken up to 0.5 solar radii ($R_\odot$) above the solar limb. The multiple images are taken from the array of four telescopes seen in Figure 1 with 1.5-arcsec spatial resolution and 12-second temporal resolution. Filters on the telescopes cover ten different wavelength bands that include two ultraviolet, one visible light band and seven extreme ultraviolet (EUV) which are used in this research ($\lambda \in [94, 131, 171, 193, 211, 304, 335]$ Å).

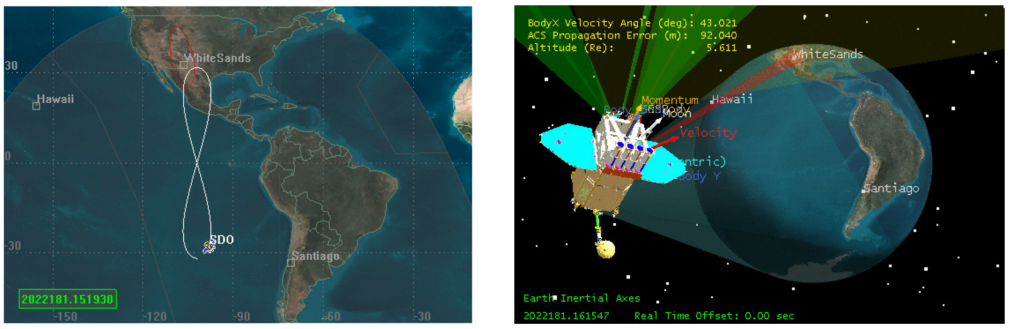

(a) The elongated figure-eight orbit as it is viewed by SDO's ground station.

(b) SDO's orbit allows its high-gain antenna to maintain continuous contact with NM.

Figure 2: Relying on a single site (White Sands, NM) reduces the complexity of the ground system, offering rapid cadence and continuous coverage required for the SDO science observations.

.

SDO is in a circular geosynchronous orbit (6.6 Earth Radii) inclined by 28.5° which allows the spacecraft to maintain nearly continuous contact with a ground station in White Sands, New Mexico, avoiding implementation of sophisticated techniques such as combining data from multiple and widely spaced antennas scattered around the globe. The

inclined orbit enables SDO to reduce the number of eclipses when it passes through the Earth's night side. The SDO orbit ranges from about 32° North to 32° South in latitude and is at 108° West longitude. When viewed from the ground station, the orbit resembles an analemma (elongated figure eight) as it orbits the Earth once per day. The orbit of the SDO will be discussed again in Section 5 when compared to the orbit of GOES-14.

3 AIA Spike Data

The AIA investigation applies a "despiking" algorithm (Lemen et al., 2011) to all EUV Level-1 data in order to remove brightened pixels that result, primarily, from the local particle population at SDO's geosynchronous location. A typical 304 Å image, for example, contains over 50,000 "despiked" pixels (0.3% of 16 Megapixels), but the number can be in the millions during periods of enhanced particle flux. Without the despiking algorithm, several AIA images would be unreliable for scientific purposes. The despiking algorithm, however, does not always distinguish between compact brightenings of solar (photon) origin and particle hits.

Each AIA Level-1 image has an associated "spikes.fits" file containing the removed spike data, so that a user can restore them in an image if some of the spikes were of solar origin (such as the case of the P. Young et al. (2013) flare kernels and the P. Young & Muglach (2014) coronal hole jets). However, an investigation of the compact brightenings by Kirk et al. (2017, 2014) showed that fewer than 0.1% of the spikes are of real solar (photon) origin (P. R. Young et al., 2021). Therefore, the "spiked pixels" observed over the course of the SDO mission so far are predominantly of magnetospheric origin, presenting a rich data resource that can be used to examine particle source populations. As there are over 200 million AIA images, this represents an extensive data set, with an estimated 6×10^{12} pixel hits over the course of twelve years of operation.

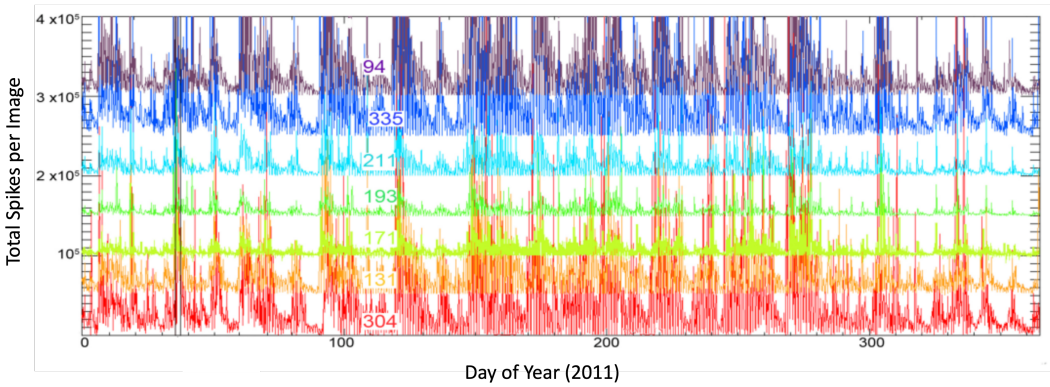

Figure 3: Number of AIA despiked pixels per 16-megapixel image for the year 2011. The 304 Å numbers are to scale; other wavelengths are offset by multiples of 50,000 to enhance visibility.

Figure 3 shows the number of spiked pixels in each of the seven AIA EUV passbands over the course of 2011. It is noteworthy that: 1) the number of spikes per image can vary greatly not only in time, but from wavelength to wavelength, and 2) while there is some correlation between enhanced periods from one day to the next, the degree of enhancement can vary greatly. To determine the nature of a particular spike, there are several factors at play, including the detectability of the spike against the background solar signal.

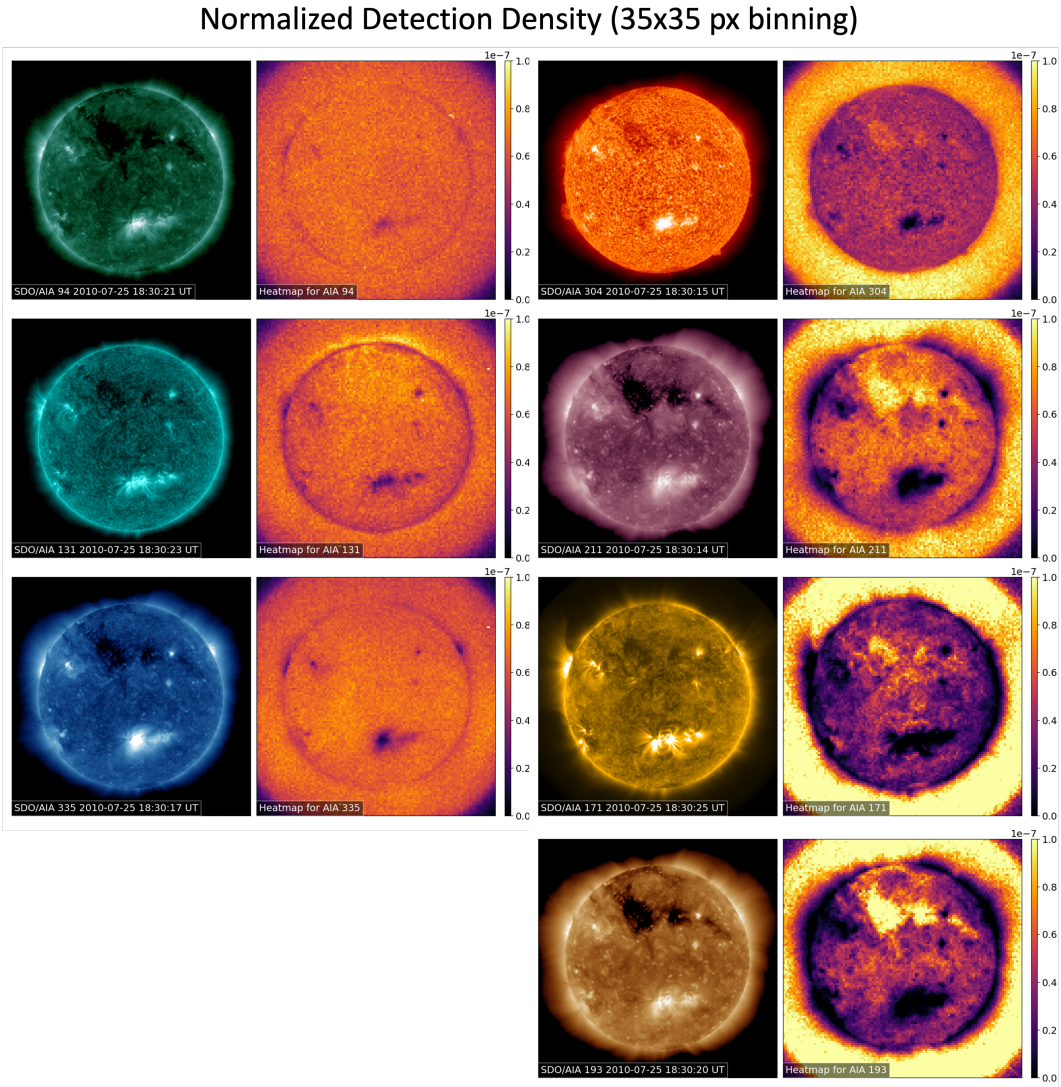

Figure 4: NSPIKES detection density maps are shown alongside the seven AIA EUV wavelengths on 2010-07-25, to indicate the non-uniformity of NSPIKES detection in the images. The detection density maps are assembled from one hour of NSPIKES data, then normalized so that the total integrated NSPIKES flux is equal to unity on the map. The wavelengths 94, 131, 335 Å show some correlation with solar structure in the image. However, the other wavelengths are much more strongly influenced by solar structure, and the detection density maps appear as "negatives" of the original images.

Figure 4 demonstrates the influence of solar structure on the detection of spikes. The seven AIA EUV wavelengths are shown alongside a map of NSPIKES detection density for each passband. Some wavelengths have NSPIKES detection densities that are more smoothly distributed across the image (94, 131 and 335 Å), while others have high variation in NSPIKES flux that are anticorrelated with coronal structure (171, 193 and 211 Å). The dark coronal hole region on the disk shows up as a bright region in the spikes detection map, while the bright active region is dark in NSPIKES. The 304 Åimage has intermediate behavior between the two groups: the on-disk detection is consistently suppressed while the off-limb detection is smooth and strong. Since the location of magnetospheric particle hits on the detector should not correlate with solar features, the higher spike densities in dark regions are due to the AIA algorithm's likelihood of identifying a spike.

Rather than exploring the nature of the different spikes, the present research effort utilizes the outcome of the AIA investigation algorithm — the number of spikes (namely the NSPIKES header on SDO's metadata) detected in every single EUV image — as is. However, by studying the variation of NSPIKES through time and comparing it with the geomagnetic indices and the particles detected by the GOES-14 instruments we can gain information about the nature of the spikes.

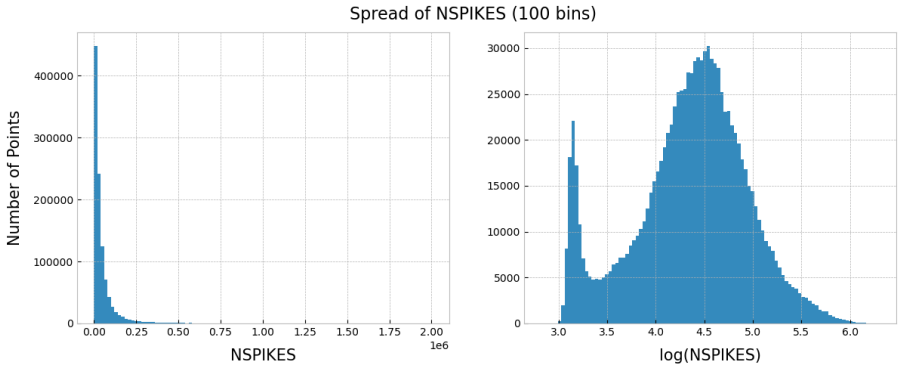

Figure 5: Histograms where the number of spikes in each AIA 304 Å image are put in 100 bins. The left histogram shows the distribution of the NSPIKES data, while the right histogram shows the distribution of the NSPIKES values in a logarithmic scale. In both plots, linear bins are being used (the entire range of values is divided into a series of equal-size intervals) resulting in the graphs having different scales.

Figure 5 shows the number of spikes in a histogram distribution of a series of 100 intervals ("bins"). The overwhelming majority of the NSPIKES falls into the first twelve bins with values that range from 0 to 250,000. However, in rare occasions, AIA images can contain up to 2,000,000 spikes. To deal with these outlier values, we often use the logarithm of NSPIKES which yields two Gaussian distributions (a narrower for low NSPIKES values and a wider for regular ones) of the data as seen in the right histogram. The first Gaussian distribution that appears at the logarithmic histogram is for an NSPIKES range between 1000 and 1500. We find that this lower value distribution represents spikes detected at the highest and lowest latitudes of the SDO orbit, therefore it represents readings in the magnetospheric cusp. Although this first distribution can be found useful for characterizing the open field lines of the upper and lower magnetosphere, in this study we focus on correlations within closed field regions of the magnetosphere, and only use NSPIKES values that are greater than 1500. This lower value NSPIKES distribution will be further discussed in Section 7 as it is useful material for future studies. In the next

chapter we will be comparing the NSPIKES values (≥ 1500) above with a) three geomagnetic indices and b) with the particles detected by three GOES-14 instruments.

4 Correlation with Geomagnetic Parameters

The preliminary study described in this Section suggests that there is some correlation between geomagnetic parameters and the number of spikes seen in the AIA images. The geomagnetic parameters that were investigated are Sym-H and K-index (from which Kp and ap are derived).

Sym-H (abbreviation for symmetric disturbance of horizontal geomagnetic fields) is a proxy of the axially symmetric magnetic field disturbance at low and middle latitudes on the Earth's surface measured in nano-Tesla (nT). Sym-H is an important index for space weather as it indicates the intensity of a magnetic storm similarly to Dst (Wanliss & Showalter (2006)) but with a much higher time resolution (1 minute cadence). It is recorded every one minute and in our study it varies mainly from 50 (quiet) to -200 (average intensity magnetic storm as discussed by Cai et al. (2009)).

K-index is quasi-logarithmic local index of the 3-hourly range in magnetic activity relative to an assumed quiet-day curve for a single geomagnetic observatory site. Menvielle & Berthelier (1991); Matzka et al. (2021) explain how Kp is derived from the mean standardized K-index readings from 13 geomagnetic observatories between 44 degrees and 60 degrees northern or southern geomagnetic latitude and is designed to measure solar particle radiation by its magnetic effects. The scale of Kp ranges from 0 to 9 and is expressed in thirds of a unit using a plus or minus sign for notation (e.g. 5- is 4 2/3, 5 is 5 and 5+ is 5 1/3). Using Kp, a linear equivalent is derived, the ap index, which ranges from 0 to 400 and is also calculated in 3-hour intervals (Rangarajan & Lyemori (1997)).

To evaluate the correlation between the NSPIKES variable and the different geomagnetic parameters we use two different coefficients, the Pearson Correlation Coefficient (Pearson, 1896) and the Spearman's Rank Correlation Coefficient (Spearman, 1961). The Pearson coefficient (r) is a measure of linear correlation between two sets of data. The r coefficient is defined as the ratio between the covariance of two variables and the product of their standard deviations. It is essentially a normalized measurement of the covariance and therefore takes values between -1 and 1. If $r > 0$ then there is positive association and if $r < 0$ there is a negative association, that is, as the value of one variable increases, the value of the other variable increases or decreases respectively. An $r = 0$ means that there is no association between the two variables. On the other hand, the Spearman coefficient (ρ) assesses how well the relationship between two variables can be described using a monotonic function. More specifically, ρ is equal to the Pearson correlation between the rank values of those two variables. Similar to r, a perfect Spearman correlation of 1 or -1 occurs when each of the variables is a perfect monotone function of the other. The Pearson and Spearman coefficients will be used throughout the paper as a measure of correlation between parameters.

The first plot on the top part of Figure 6 presents the number of spikes detected in all seven wavelengths of the AIA instrument against time. We plot the data for the entirety of 2019 taking 3 hour averages to match the geomagnetic parameters cadence (SDO has an 12 second cadence therefore we take the average of about 1000 SDO data points). The second, third and forth plots on top are the ap, Kp and Sym-H index values against time for the same interval, respectively. It can be easily observed that when there is an increase on the NSPIKES parameter on the top part of Figure 6, the geomagnetic parameters Kp and ap increase while Sym-H decreases. The correlation between NSPIKES and the geomagnetic parameters is even more evident when looking into a single month. On the bottom left part of Figure 6 a comparison of the number of spikes with the geomagnetic parameters is performed for the second month (Februrary) of 2019.

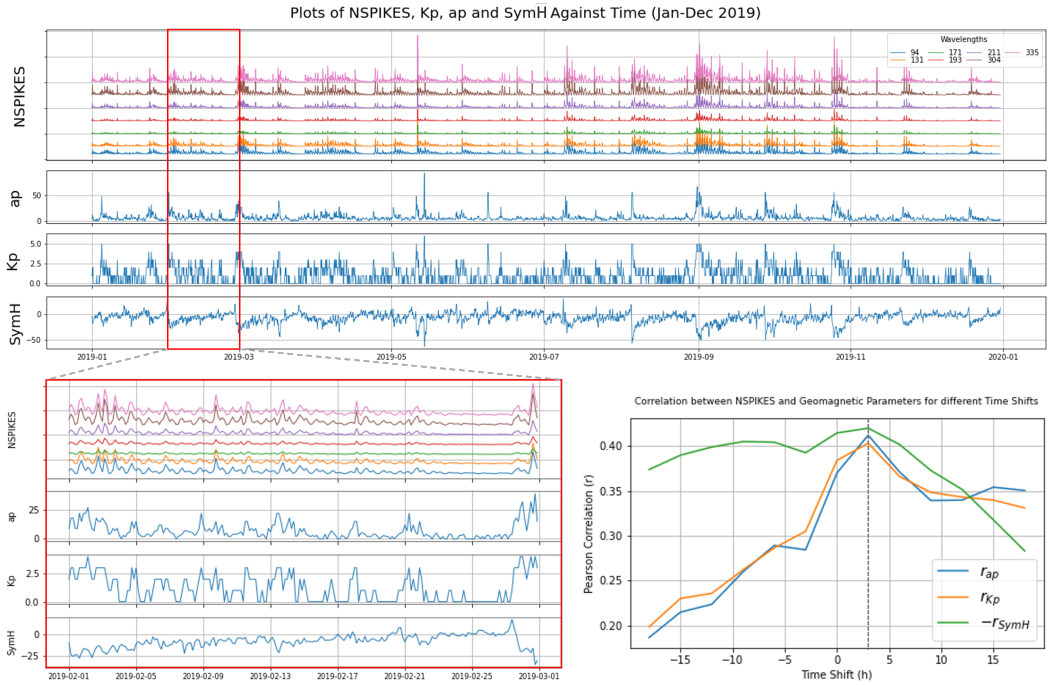

Figure 6: The top panel shows a timeline of the seven different AIA wavelength NSPIKES along with the geomagnetic parameters Sym-H, Kp and Ap for the entire year of 2019. The bottom left panel presents the timeline for the month of February 2019. The bottom right panel shows the Pearson Correlation values for different time shifts of the NSPIKES timeline.

Similarly, it is observed that an increase of Kp and ap (or decrease for Sym-H) is followed by a corresponding increase in the number of spikes. The increased spikes values at the beginning and the end of the month are a representative example. Indicative of this relationship are the values of the Pearson and Spearman coefficients calculated. For the month of February 2019, NSPIKES (335 Å) yields an $r = 0.52$ and a $\rho = 0.53$ when compared against Kp, an $r = 0.50$ and a $\rho = 0.53$ when compared against ap while an $r = -0.46$ and a $\rho = -0.46$ when compared against Sym-H (negative correlation). Similarly, for the entire year of 2019, NSPIKES (335 Å) yields an $r = 0.39$ and a $\rho = 0.37$ when compared against Kp, an $r = 0.37$ and a $\rho = 0.39$ when compared against ap and an $r = -0.42$ and a $\rho = -0.38$ when compared against Sym-H.

The time lag between the geomagnetic parameters drop or increase with the corresponding increase of NSPIKES observed during the month of February 2019 is studied in the bottom right plot of Figure 6. More specifically, seven positive and seven negative 3 hour (time cadence) shifts are performed on the NSPIKES data and the different Pearson correlation coefficients are calculated for each shift. A positive lag (shift) means that Kp leads NSPIKES by $\Delta t \in [3, 6, 9, 12, 15]$h while a negative lag means that NSPIKES leads Kp by the same Δt time intervals. The highest correlation value is recorded for a positive 3 hour shift and it can be assumed to be of no significance -especially for Kp and ap- as the parameters are a 3 hour standardized mean. For studies where a more accurate time-shift value is needed, higher-resolution Kp, ap and Sym-H data of longer time spans (compared to only a month used here) can be utilized to determine an exact $\Delta t \leq 3h$.

Wavelength (Å)	94	131	171	193	211	304	335
				Pearson Correlation (r)			
Kp	0.262 ± 0.12	0.285 ± 0.09	0.346 ± 0.03	0.312 ± 0.11	0.307 ± 0.11	0.341 ± 0.05	0.284 ± 0.13
ap	0.227 ± 0.12	0.248 ± 0.09	0.305 ± 0.06	0.273 ± 0.10	0.265 ± 0.11	0.297 ± 0.06	0.243 ± 0.13
SymH	0.265 ± 0.12	0.285 ± 0.09	0.326 ± 0.05	0.292 ± 0.10	0.293 ± 0.11	0.321 ± 0.05	0.266 ± 0.13
				Spearman Correlation (ρ)			
Kp	0.264 ± 0.04	0.258 ± 0.04	0.309 ± 0.04	0.312 ± 0.04	0.306 ± 0.04	0.315 ± 0.04	0.314 ± 0.04
ap	0.274 ± 0.04	0.268 ± 0.04	0.323 ± 0.04	0.326 ± 0.04	0.319 ± 0.04	0.328 ± 0.04	0.327 ± 0.04
SymH	0.296 ± 0.04	0.292 ± 0.04	0.322 ± 0.03	0.324 ± 0.03	0.323 ± 0.03	0.329 ± 0.03	0.328 ± 0.03

Table 1: Ten year (2011-2021) mean Pearson and Spearman correlation coefficients for NSPIKES when compared with the three geomagnetic parameters (Kp, ap and Sym-H) for the seven different AIA wavelengths. In blue are marked the highest correlation values for each one of the geomagnetic indices.

The Pearson and Spearman correlation coefficients for the seven different NSPIKES passbands ($\lambda \in [94, 131, 171, 193, 211, 304, 335]$ Å) when compared to the three different correlation coefficients (Kp, ap and Sym-H) are presented in Table 1. The results presented are the mean of the yearly correlations for a ten year period (2011-2021). The highest values (marked in blue) for ap and Sym-H are the Spearman's correlations observed for $\lambda = 304$ Å. For Kp the Pearson linear correlation scores for $\lambda = 171$ Å is the highest value. Note that for the Sym-H parameter only the absolute values of r and ρ are recorded as its correlation to NSPIKES is negative. In the next chapters a similar analysis will be performed when the NSPIKES are compared to the readings of the GOES-14 electron and proton detection instruments.

5 Correlation with GOES-14 Data

As mentioned in Section 2, SDO is in a circular geosynchronous orbit at an altitude of 35,789 km (22,238 mi), at 102° West longitude, inclined at 28.5°. This means that twice a day SDO passes through the equator where it comes in very close proximity ($\gtrapprox$ 1,642 km) to the GOES-14 satellite which is in a geostationary orbit at 105° West longitude at an altitude of 35,773 km (22,228 mi). This means that twice a day we get a chance to compare the SDO spike data with the GOES-14 proton and electron readings.

Figure 7 shows the orbits of the SDO (blue) and GOES-14 (orange) satellites in the Geocentric Equatorial Inertial System (GEI), while in red is the part of the orbits where the two satellites "meet". In the rest of the paper we will be denoting as "Equator Data" the SDO and GOES-14 readings obtained at the part of the orbits highlighted in red. The GEI system has its x-axis pointing from the Earth towards the first point of Aries (the position of the Sun at the vernal equinox). This direction is the intersection of the Earth's equatorial plane and the ecliptic plane and thus the x-axis lies in both planes. The z-axis is parallel to the rotation axis of the Earth and y completes the right-handed orthogonal set.

GOES-14 (known as GOES-O prior to reaching its operational orbit) is a weather satellite, which was built by Boeing and is part of the US National Oceanic and Atmospheric Administration's (NOAA) Geostationary Operational Environmental Satellite (GOES) system. It is equipped with nine different instruments including the EPS/HEPAD (Energetic Particle Sensors / High Energy Proton and Alpha Detector, Hanser (2011)) which is part of the overall SEM (Space Environment Monitor) and whose data is used in this research. The EPS consists of two energetic proton, electron and alpha detectors

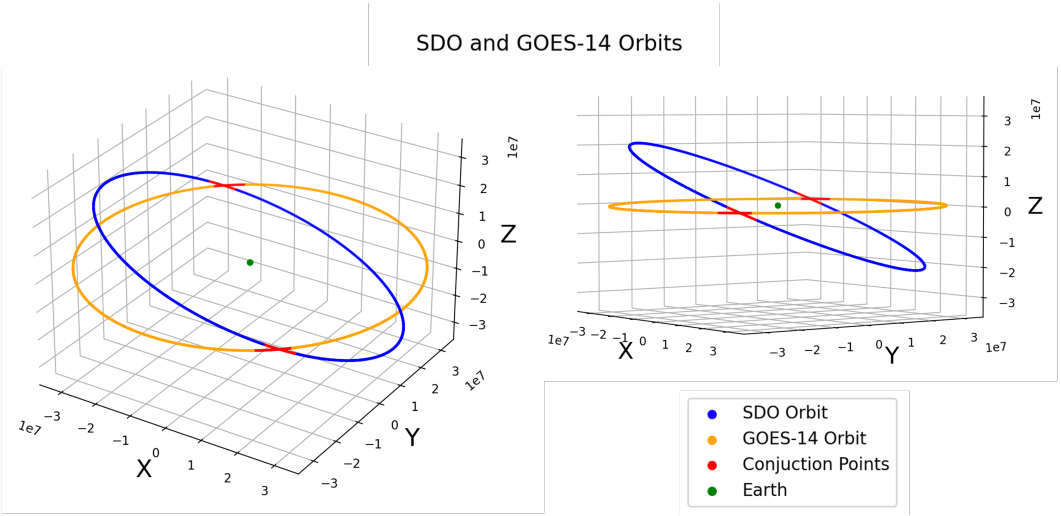

Figure 7: Three-dimensional plot of the SDO (blue) and GOES-14 (orange) orbits in the GEI coordinate system. In red are the conjunction parts of the orbits ($z_{SDO} = \pm 2,000$km) and in green is the center of the coordinate system, the Earth.

(EPEAD), a magnetospheric proton detector (MAGPD) and a magnetospheric electron detector (MAGED). The data from all three detectors are used in this research to calculate their readings' correlations with the SDO NSPIKES values and explore the nature of the AIA spikes.

This equator region where the orbits intersect is at the geographic equator. This is generally close to the latitude of minimum magnetic field strength for each field line. Under the dipole model and non-dipolar typical geomagnetic conditions, this is at the magnetic equator. This latitude of minimum magnetic field strength has the property that mirroring radiation belt particles of all pitch angles will pass through it at some point during their bounce motion. While not exactly at the latitude of minimum magnetic field strength, we are close to it. This gains us the insight that the satellite is exposed to nearly all bouncing particles from this location, with detections limited only by the field-of-view of the virtual detector.

5.1 NSPIKES Correlation with Electrons

The Magnetospheric Electron Detector (MAGED) is a set of nine collimated solid state telescopes (Rowland & Weigel, 2012) each with a 30° full-angle conical field of view, that form a cruciform field of regard with the central telescope pointing anti-earthward. The telescopes collect magnetospheric electrons and provide electron flux measurements in five energy channels that range from 30 keV to 600 keV (30–50, 50–100, 100–200, 200–350, and 350–600 keV). For each channel the number of electrons is counted in units of $e^-/(cm^2$ sr keV s). The MAGED archival flux data are provided as directional differential electron fluxes determined for the midpoint of the five energy ranges (i.e., at 40, 75, 150, 275, and 475 keV, (Sillanpää et al., 2017)).

Figure 8 shows how the SDO NSPIKES and GOES-14 Electron Flux values in logarithmic scale vary against time for a single day (August 22, 2018), along with the corresponding SDO Latitude (z-axis) values at each moment (1m cadence). As equator data (red in Figure 7) we chose the data at the times where SDO passes through the equator, i.e. the times where SDO is within 2000 km from the equator ($z_{SDO} = \pm 2000$ km).

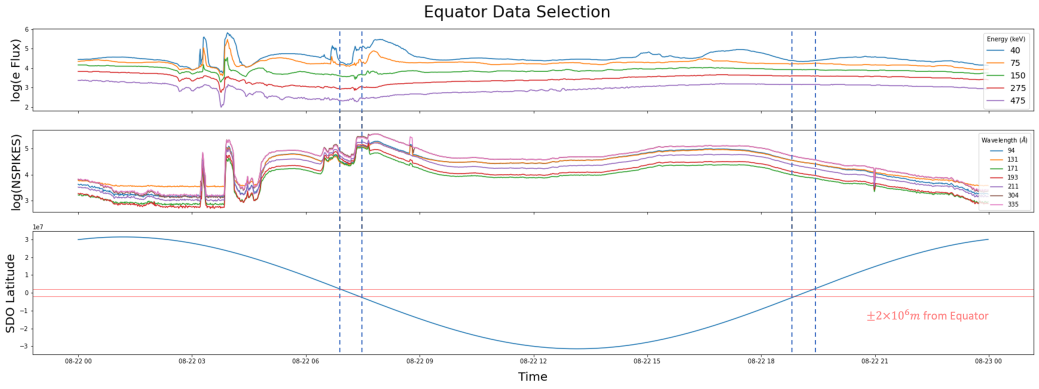

Figure 8: Plots of the GOES-14 MAGED Electron Flux (Telescope 2) and the SDO NSPIKES in logarithmic scale and the SDO Latitude against time for a single day (August 22, 2018). The horizontal dotted lines define the latitude interval in which Electron Flux and NSPIKES values will be considered as "Equator Data".

Therefore, the correlation analysis presented below will be done for three different domains: first we analyze the entirety of the NSPIKES and Electron Flux data (Full Orbit), we then concentrate only on assessing the correlation of the data intervals that lie between the dotted lines of Figure 8 (Equator) and lastly for comparison reasons we also compute the correlation for the times where SDO is not in close proximity to GOES-14 (Non-Equator).

MAGED Electron Flux	**40 keV**	**75 keV**	**150 keV**	**275 keV**	**475 keV**
			Pearson Correlation (r)		
Equator	0.745 ± 0.023	0.678 ± 0.033	0.479 ± 0.061	0.357 ± 0.069	0.304 ± 0.070
Non-Equator	0.584 ± 0.040	0.587 ± 0.044	0.491 ± 0.057	0.394 ± 0.055	0.322 ± 0.052
Full Orbit	0.587 ± 0.039	0.587 ± 0.043	0.488 ± 0.057	0.391 ± 0.055	0.320 ± 0.053
			Spearman Correlation (ρ)		
Equator	0.729 ± 0.009	0.712 ± 0.011	0.670 ± 0.025	0.611 ± 0.036	0.550 ± 0.039
Non-Equator	0.529 ± 0.017	0.526 ± 0.007	0.499 ± 0.004	0.456 ± 0.010	0.412 ± 0.013
Full Orbit	0.534 ± 0.016	0.530 ± 0.006	0.504 ± 0.004	0.460 ± 0.011	0.416 ± 0.014

Table 2: Pearson and Spearman correlation values for NSPIKES and MAGED Electron Flux data for the five different MAGED energy channels, calculated over a period of 27 months (December 2017 to February 2020). The nine different MAGED telescopes and seven different AIA wavelengths are accounted for by presenting the mean and standard deviation of all possible combinations. In blue, are marked the highest correlation values for each different SDO and GOES satellite location.

To determine the origins of the spikes in the AIA images, we first study the association of the NSPIKES parameter with the MAGED Electron Flux data. Table 2 presents the Pearson and Spearman correlation values between NSPIKES and MAGED Electron Fluxes for the entire uninterrupted period when SDO and GOES-14 were both operational (December 2017 to February 2020). For each one of the five different MAGED chan-

nels, the mean value and standard deviation for all different combinations of MAGED telescopes and AIA wavelengths is recorded. Separate correlations are also calculated for the Equator and Non-Equator periods as seen and described in Figure 7.

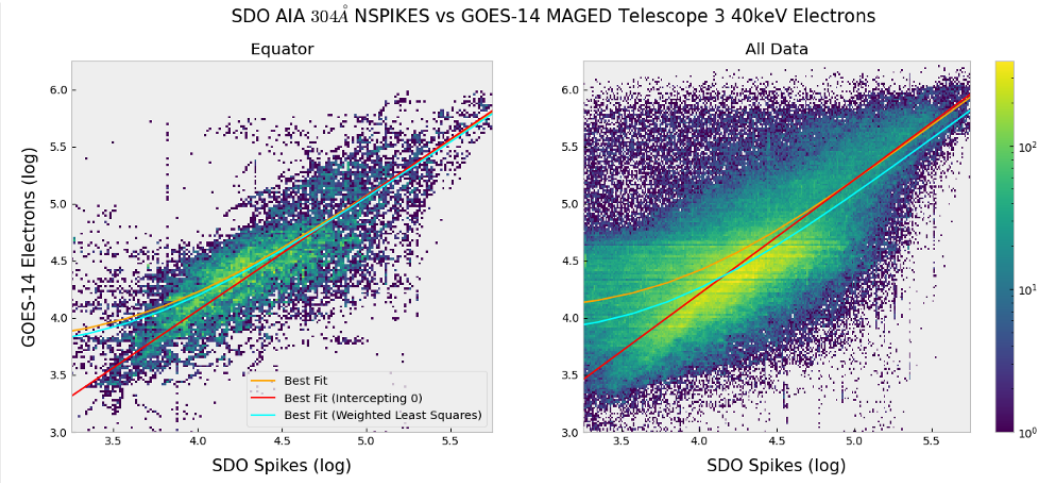

Figure 9: Heatmaps for the Equator and Full Orbit NSPIKES and MAGED Electrons data in logarithmic scale. The correlation values for the Equator data are $r = 0.779$ and $\rho = 0.731$.

For most of the cases studied, the Spearman correlation values are higher than the respective Pearson ones suggesting that the relationship between NSPIKES and MAGED Electron Fluxes is not exactly linear but it can better be described by a monotonically increasing function. Low energy electrons (ex. 40 and 75 keV channels) show always higher association with NSPIKES. Hence, the low energy MAGED electron channel of 40 keV is the one that can be better associated with NSPIKES having a Pearson correlation of $\rho = 0.745 \pm 0.023$ and a Spearman correlation of $\rho = 0.729 \pm 0.009$ at the equator. Lastly, as expected due to the SDO and GOES-14 satellites being in close proximity and therefore study the same space within the radiation belt, the Equator correlation values are most of the times higher than the Non-Equator ones by $\Delta\rho = 0.170$ and $\Delta r = 0.021$ ($\rho_{eq} - \rho_{non} = 0.170 \pm 0.022$ and $r_{eq} - r_{non} = 0.021 \pm 0.057$). It is noteworthy that for satellite data which are prone to a significant amount of noise, a Pearson and Spearman value greater than 0.5 can be considered as a relatively strong correlation.

Although Table 2 presents the mean values across different MAGED telescopes and AIA wavelengths, there are specific cases where the association between NSPIKES and MAGED electrons can be even higher. One of these cases is when we compare the number of spikes detected in the $\lambda = 304$ $\AA$ AIA images to the 40 keV electrons detected by the third MAGED detector (Telescope 3) from December 2017 to February 2020. Figure 9 includes the two dimensional histograms (heatmaps) for these specific NSPIKES and MAGED electron values, both for the full orbits (a) and the equator intervals (b).

On the left heatmap of Figure 9 the Equator AIA 304 Å NSPIKES are put in 300 bins and are plotted against the respective MAGED Telescope 3 40 keV Electrons (also split in 300 bins) in logarithmic scale for the time period between December 2017 to February 2020. The right heatmap presents the same data but for the full satellite orbits. The Pearson and Spearman values for the Equator data are $r = 0.779$ and $\rho = 0.731$ respectively. All plots include the best fit lines in orange, the best fit lines forced to inter-

cept $(0, 0)$ in red and the weighted ($w = 1/x$) least squares lines in cyan. The trend where Equator data associate better with each other holds true for this case too.

The issue of the bias in the correlation is dealt with carefully. It is possible that spikes originate from multiple, independent processes. In addition to the source of radiation belt particle impacts, other sources could include (a) arcing due to differential charging or (b) galactic cosmic rays impacts. Processes such as (a) or (b) will necessarily generate spikes at a constant background level when averaged over these several years. This is due to their independence from the radiation belt enhancements: radiation belt enhancements do not contribute to differential charging, and the galactic cosmic ray arrival rate does not depend strongly on either radiation belt enhancements or magnetospheric reconfigurations. Therefore, they collectively would appear in Figure 9 as a constant bias term. Because we do not know for sure whether these additional possible sources arise in reality, we model with and without a bias term. Here we need to note that by definition, modeling with bias in Figure 9 means expressing the distribution as a best fit line that intercepts 0 (in red), whereas the rest of the fitted lines constitute modeling without bias.

EPEAD (800 keV)	Spearman Correlation (ρ)						
Wavelength (Å)	**94**	**131**	**171**	**193**	**211**	**304**	**335**
Equator	0.529	0.534	0.432	0.435	0.456	0.448	0.447
Non-Equator	0.383	0.385	0.350	0.350	0.357	0.350	0.350
Full Orbit	0.387	0.389	0.351	0.352	0.359	0.352	0.352

Table 3: Spearman correlation values for NSPIKES and EPEAD $>$ 0.8 MeV (E1) electron flux data for the seven different AIA wavelengths, calculated over a period of 27 months (December 2017 to February 2020).

The second electron-detecting instrument onboard of GOES-14 is the Energetic Proton Electron and Alpha Detector (EPEAD), which observes electrons in the energy range above that of MAGED. There are two EPEADs on GOES-14, one with a field-of-view (spacecraft $+x$ direction) to the east, and the other with field-of-view to the west (spacecraft $-x$ direction). The results that the two EPEADS yield when compared to the NSPIKES are almost identical therefore for simplicity in this report we only present the EPEAD East results. More specifically, EPEAD East gives us the dead-time corrected average flux of electrons from the E1 channel with effective energy $>$ 0.8 MeV with backgrounds and proton contamination removed (if contamination is too severe, fluxes are replaced with fill values, but this is rare in the E1 channel). EPEAD also measures $>$ 2 MeV and $>$ 4 MeV electron fluxes. However, because these channels exhibit extended periods when the electron fluxes are below backgrounds, they were not used in the correlation analysis.

The relationship between SDO NSPIKES and EPEAD Electrons is highly non-linear therefore Table 3 presents only the Spearman Correlation values for different AIA wavelengths. Similarly to the MAGED data, the EPEAD Electron data correlates better with SDO's NSPIKES at the equator compared to the rest of the orbit, showing an increase in Spearman correlation of $\Delta\rho = \rho_{eq} - \rho_{non} = 0.108 \pm 0.026$. Out of the seven AIA wavelengths, the best association between the two data products is for $\lambda = 131$ Å where $\rho = 0.534$ at the SDO and GOES-14 orbits conjunction points.

For completion, Table 4 presents the same results as Table 3 does, but for the lowest energy channel available the MAGED data provides (40 keV). For the equator data, it is important to note a) the increase in correlation when using lower energy channels

MAGED ($40keV$)	Spearman Correlation (ρ)						
Wavelength (Å)	**94**	**131**	**171**	**193**	**211**	**304**	**335**
Equator	0.712	0.713	0.735	0.721	0.729	0.731	0.737
Non-Equator	0.491	0.499	0.532	0.531	0.524	0.532	0.534
Full Orbit	0.501	0.509	0.538	0.536	0.535	0.545	0.541

Table 4: Spearman correlation values for NSPIKES and MAGED $40keV$ electron flux data for the seven different AIA wavelengths calculated over a period of 27 months (December 2017 to February 2020). The values represent the mean for nine different MAGED telescopes with a very low standard deviation $\leq \pm 0.04$.

and b) the decrease in standard deviation for the different wavelength results ($\rho_{800keV} = 0.468 \pm 0.044$ and $\rho_{40keV} = 0.725 \pm 0.010$). When comparing the Equator data with the Non-Equator and the Full-Orbit data, the same trends as in the rest paper apply to the MAGED (40 keV).

In conclusion, this section shows that the SDO AIA NSPIKES header variable associates very well with the electron readings from two different GOES-14 detectors, the MAGED and the EPEAD, especially when the two satellites are in close proximity twice a day. The evidence suggest that the spikes detected in the SDO's AIA images are caused by energetic electrons that reside within the radiation belt. In the next Section we will do a similar analysis for magnetospheric protons and also evaluate the NSPIKES during the three largest Solar Energetic Particle (SEP) events the SDO satellite has witnessed.

5.2 NSPIKES Correlation with Protons

The third GOES-14 detector whose data we compare to the SDO AIA spikes is the Magnetospheric Proton Detector (MAGPD). Similar to MAGED, MAGPD has nine telescopes with fields-of-view at the –Z direction, pointing away from the earth. The instrument collects magnetospheric protons and provides proton flux measurements ranging from 80 keV to 800 keV in five separate channels which have mean flux detection values of 95, 140, 210, 300 and 575 keV and are corrected for dead time.

Similarly to the MAGED and EPEAD instruments, for all the different cases studied in Table 5, the Spearman correlation values are higher ($\rho - r = 0.180 \pm 0.040$) than the respective Pearson ones, suggesting that the relationship between NSPIKES and MAGPD Proton Fluxes is not linear either and it can be better described by a monotone function. Note that the MAGPD $\rho - r$ is higher compared to MAGED, with proton Pearson results being in the majority of the studies < 0.2 suggesting that there is no significant linear correlation. High energy protons (ex. 300 and 575 keV channels) show always higher association with NSPIKES. Hense, the second highest energy MAGPD proton channel of 300 keV is the one that can be better associated with NSPIKES having a Spearman correlation of $\rho = 0.467 \pm 0.0476$ at the equator. Lastly, as observed in all the studies in Section 5.1, the Spearman correlation Equator values are always higher than the Non-Equator ones by $\Delta\rho = \rho_{eq} - \rho_{non} = 0.056 \pm 0.030$.

Although the Spearman correlation values for the MAGPD protons are in the majority of the case studies inferior to the ones calculated for the MAGED and EPEAD electrons, a Spearman value of $\rho \in [0.3, 0.5]$ suggests that there is some correlation. However, the MAGPD energies are up to two orders of magnitude lower than the proton energies that typically cause spikes in images (Didkovsky et al., 2006). To investigate whether protons in the MeV energy range, that is typically associated with spikes in solar im-

MAGPD Proton Flux	**95 keV**	**140 keV**	**210 keV**	**300 keV**	**575 keV**
	Pearson Correlation (r)				
Equator	0.132 ± 0.083	0.156 ± 0.091	0.190 ± 0.101	0.211 ± 0.117	0.192 ± 0.106
Non-Equator	0.149 ± 0.069	0.173 ± 0.080	0.201 ± 0.096	0.234 ± 0.107	0.212 ± 0.098
Full Orbit	0.148 ± 0.070	0.172 ± 0.081	0.209 ± 0.096	0.233 ± 0.108	0.211 ± 0.098
	Spearman Correlation (ρ)				
Equator	0.326 ± 0.052	0.357 ± 0.052	0.423 ± 0.050	0.467 ± 0.0476	0.447 ± 0.042
Non-Equator	0.306 ± 0.019	0.329 ± 0.018	0.370 ± 0.017	0.389 ± 0.016	0.345 ± 0.014
Full Orbit	0.305 ± 0.020	0.328 ± 0.019	0.370 ± 0.018	0.390 ± 0.017	0.347 ± 0.015

Table 5: Pearson and Spearman correlation values for NSPIKES and MAGPD Proton Flux data for the five different MAGPD energy channels, calculated over a period of 27 months (December 2017 to February 2020). The nine different MAGPD telescopes and seven different AIA wavelengths are accounted for by presenting the mean and standard deviation of all possible combinations. In blue are marked the highest correlation values for each different SDO and GOES satellite location.

ages (e.g., SOHO EIT), contribute to AIA spike data, we study the fluctuation of the NSPIKES variable during large Solar Energetic Particle (SEP) events of Solar Cycle 24.

Figure 10 shows the evolution of the NSPIKES (304 Å) variable during the three most significant (highest proton flux at > 10 MeV) SEP events that NOAA observed (Rodriguez et al., 2014) since the beginning of the SDO mission (July 2010). Such events have been thoroughly studied (Cliver, 2008; Reames, 2013) and used before in space weather prediction applications (Whitman et al., 2022; Kasapis et al., 2022). Research has shown (Lanzerotti, 1968; G. A. Paulikas & Blake, 1969; Fillius, 1968) that during such events, the proton content in the earth magnetosphere increases drastically which would mean that spikes due to protons in SDO's AIA images would increase too (Lario, 2005; Matthiä et al., 2009; Kress et al., 2013; Rodriguez et al., 2010). As it can be observed in Figure 10, the NSPIKES data does not show any significant increase during the beginning (green dotted lines) nor during the maximum (red dotted lines) of these three significant SEP events as it has been recorded by GOES-13 based on proton flux (yellow). We note that there is a brief period around 2012-Jan-24T15:30 during which a strong magnetospheric compression occurred. The 30-600 keV radiation belt electron flux (not shown) increased due to the compression, while the increase in the ongoing solar particle event fluxes was due to acceleration by the shock prior to arrival at Earth. SDO was at the highest latitude in its orbit. This analysis indicates that spike correlation with proton flux may be an inherited (non-causal) correlation due to the fact that regions of high electron fluxes in the magnetosphere can also have high proton fluxes.

6 Discussion

The association of the SDO spike data with the GOES-14 electrons and proton fluxes is especially useful for characterizing the radiation belt at non-equatorial latitudes where measurements are not available. Solar research, which uses data from satellites such as SOHO, has measured direct proton hits on CCD cameras (Didkovsky et al., 2006) within and outside the solar disk. Unlike SOHO, which orbits around the first Lagrangian point (L1), SDO's geosynchronous orbit intersects the outer radiation belt, indicating electron hits should be considered too.

In Table 3, the correlations with the > 0.8 MeV electrons are significantly higher for the two EUV wavelengths (94 and 131 Å) that have transmissive zirconium (Zr) fil-

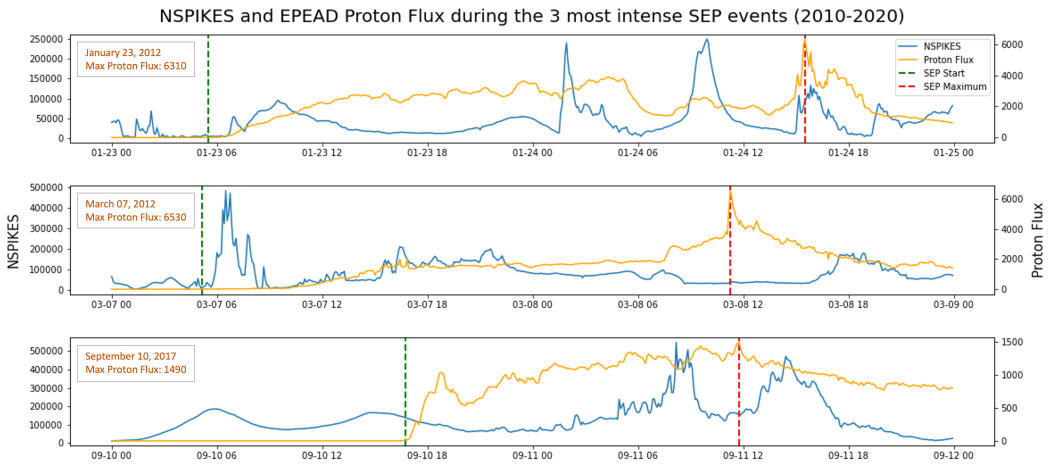

Figure 10: NSPIKES at 304 Å (blue) and EPEAD > 10 MeV proton (yellow) time profiles for the two-day periods that include the three most significant SEP events recorded by NOAA during the first decade of operation of the SDO. The green dotted lines signify the beginning of the SEP events and the red dotted line signifies the time of maximum flux of the events as defined by NOAA.

ters at the entrance and at the detector, than for the other EUV wavelengths, which have aluminum (Al) filters. This correlation cannot be solely a function of the individual telescopes since the 94 and 131 Åimages share telescopes with the 304 and 335 Åimages, respectively (Figure 1). One possible reason for this pattern in the correlations is based on the recognition that these filters transmit 40 keV electrons. The total thicknesses of the Zr and Al filters at the entrance and detector are 4000 and 3000 Å, respectively (Lemen et al., 2011). According to the NIST ESTAR tables (Berger et al., 1984), the average path length travelled by 40 keV electrons in Al before they stop is 3.90×10^{-3} g cm^{-2} or 48 times the thickness of the two Al filters, while the average path length travelled by 40 keV electrons in Zr is 5.19×10^{-3} g cm^{-2} or 20 times the thickness of the two Zr filters. The Zr filters thus stop more 40 keV electrons than the Al filters. If the spikes are due to electrons penetrating the filters, scattering off the mirrors and reaching the CCDs when the shutter is opened, the Zr filters suppress the signal from the 40 keV electrons more than the Al filters and thereby enhance the correlation with the $> 0.8MeV$ electrons, which are not affected significantly by the filters. This possibility should be explored quantitatively in future work.

It can be observed throughout the paper that the NSPIKES correlation tests are more sensitive to low electron energies. As it can be seen in Table 2 and Table 3, MAGED low energy electrons (ex. 40 and 75 keV channels) show always higher association with NSPIKES -regardless of the AIA EUV channel- compared to MAGED higher-energy channels and EPEAD. This might be counterintuitive as higher energy electrons should be able to penetrate the AIA telescope's protective shield easier than lower energy electrons, but our research efforts suggest that this might be a partly statistical outcome due to having many more particle hits from lower energy MAGED channels (Figure 8). The opposite trend can be observed for the MAGPD protons, where higher energy channels correlate better with NSPIKES. However, this increase may be correlative and not causative, as proton flux is correlated with electron flux.

While desirable to have, it is likely challenging to calculate a per-energy response function for the virtual electron detector from on-orbit data. However, an attempt could be made, where in the response function is modeled as a linear regression. To do this, one would model the NSPIKES variable as a linear combination of the fluxes at available energies as shown in Equation 1.

$$NSPIKES = \sum_{k=1}^{N_E} w_k \mathrm{Flux(E_k)} + \mathrm{Bias} \tag{1}$$

Here, N_E is the number of energy channels available from instrumentation and $\mathrm{Flux(E_k)}$ is the flux at energy E_k for $k \in \{1, 2, ..., N_E\}$. The response function coefficients are w_k, with k corresponding to energy E_k. These coefficients determine how much each energy-specific flux would contribute to $NSPIKES$. The Bias term models a steady background level of spikes from non-flux sources such differential charging or galactic cosmic rays. By solving for the weights in this (very) over-determined system, the response at each energy is found. Because the fluxes are correlated with each other, this regression should be done carefully and the co-variance matrix should be analyzed. Limitations to this approach are that the response function may depend on fluxes at energies not measured by GOES instrumentation.

There are studies of images that are primarily influenced by proton flux. Our results do not indicate that it is impossible for protons to also contribute to the AIA spike population. Instead, they simply indicate that the electrons have a much stronger influence because of the high energetic electron population in the Earth's magnetosphere. Studies such as Didkovsky et al. (2006) were performed using instruments in the solar wind, with different plasma environments. The focus of the paper is on determining the radiation belt measurements that correlate most highly with AIA spikes in order to use AIA as a proxy measurement. The influence of SEPs and cosmic rays is not significant at the GOES-14 Geostationary Equatorial Orbit relative to the high flux of radiation belt electrons.

In this paper, we prove that NSPIKES are a proxy for electrons (especially around the 40 keV range), therefore in future work NSPIKES can be used to a) determine the geomagnetic latitude dependence of those electrons, b) specify model plasma boundary conditions outside the geosynchronous orbit and c) see particle injections before they hit GEO. Although a strong linear correlation was found, there is some dispersion in the values. There are a number of potential factors that could contribute. First, SDO and GOES-14 are not at the exact same location, even when both were near the equator, so some difference in values can be expected. Second, SDO/AIA and GOES-14 have different detectors, and AIA was not designed as a particle detector. In Figure 4 the location of the detected spikes indicates that the spike detection algorithm is more efficient in dark regions of the image; therefore there will be some fluctuation in detection efficiency.

There is some correlation with higher electron energies and proton flux too; this study only examines correlation and not direct cause of particle hits. It is likely that different populations have contributions to the number of spikes, but the 40 keV electron flux is highest and therefore has the greatest correlation. Future studies can examine factors such as spacecraft geometry, and orientation relative to the direction of the magnetic field lines, and explicit comparison of the magnetosphere at different levels of radiation belt activity may shed more light on this. If successful, this could allow proxy measurements of electron flux at higher latitudes instead of just equatorial latitudes.

Another desirable parameter left for future analysis is that of the field of view associated with this virtual detector. This field of view would give insight into the pitch angle coverage, through coupling with a magnetic field model to provide the magnetic

field direction. Because SDO is always pointed towards the sun, the pitch angle span could be calculated geometrically from the aperture size, the CCD size, and the distance from the aperture to the CCD. We note that as SDO goes to higher magnetic latitudes, the extent will stay the same, but the center of the extent will sample a very different portion of pitch angles. Future analysis may show that this provides a natural "scanning" mechanism to gain coverage of much of pitch angle space.

Based on the results presented in this work, research in a variety of different directions could be conducted. Future work could concentrate on calculating a per-energy response function for the virtual electron detector from on-orbit data, where the response function is modeled not only as a linear regression. Additionally, in this study the electron and proton densities at the equator were discussed, but obtaining three-dimensional particle density relationships would be desirable. Therefore, studying the behavior of higher-latitude distributions and understanding the full variation of the radiation belts would be beneficial for the community.

7 Conclusion

By sampling the outer radiation belts in a range of magnetic latitudes, SDO provides unique energetic particle flux measurements. Although SDO's Atmospheric Imaging Assembly consists of solar telescopes deployed to image the Sun, AIA's CCD detector is also sensitive to direct hits from magnetospheric electrons. These impacts show up as brightenings of one to several pixels in the images that are called "spikes". As a part of data processing to create science-quality images, an algorithm removes the spikes from each of the images. The number of spiked pixels removed from the image is reported in the metadata, as a value labeled NSPIKES.

In this work we examine for the first time the behavior of NSPIKES, which is usually treated as a data artifact. We compared with global geomagnetic parameters Kp, ap, and Sym-H as a simple test to illustrate that the NSPIKES value does fluctuate with geomagnetic activity. However, the correlation was not strong; this is not surprising because the processes causing geomagnetic fluctuations and those that determine particle populations are related but not perfectly correlated.

We then examine the correlation of SDO spikes to directly measured proton and electron fluxes from the GOES-14 spacecraft which twice a day comes close to SDO (within 1700 km). We find that AIA spikes are highly correlated with the GOES-14 electrons detected by the MAGED and EPEAD instruments at the equator (where the two satellites meet) with Spearman's Correlation values of $\rho = 0.73$ and $\rho = 0.53$ respectively, while a weaker correlation of $\rho = 0.47$ is shown with MAGPD protons. In particular, it was found that the correlation was highest ($r = 0.78$) for GOES-14 MAGED 40 keV electrons, and had a linear relationship as described in Equation 2:

$$J_{GOESe,40keV} = 1.1604 \text{ NSPIKES} \tag{2}$$

This indicates that a) the SDO NSPIKES value can be used as a very good proxy measurement for 40 keV electron flux after the end of GOES-14 measurements in 2019, and b) SDO has the potential to produce electron proxy measurements far out of the ecliptic as well. In fact, sudden dropouts in the number of spikes were observed, coinciding with higher latitude passes in SDO's 28.5° inclined orbit; these periods seem to be consistent with possible locations of the polar cusp. Further examination of these flux dropout locations with geomagnetic models are planned as future work.

Boyd et al. (2021) show the correlation between two different instruments on RBSP that measure 32 keV electrons at the 90-degree pitch angle. Often, the two instuments

are at least ten times off from each other. This is about the same level of error we are seeing between our virtual NSPIKES detector and GOES. This indicates that detecting electrons using SDO data is as close to what the GOES detectors yield as two science quality instruments on the same spacecraft are to each other.

In conclusion, in this work we show that the SDO/AIA spiked pixels can help characterize the radiation belt in areas where other measurements aren't available, therefore creating a new dataset with proxy measurements from electrons of the outer radiation belt, within and out of the equator, turning the radiation belt characterization into a three-dimensional structure.

Open Research

All SDO data used in this study are available from the Joint Science Operations Center (JSOC) NASA grant (see `http://jsoc.stanford.edu/`). The GOES-14 data obtained from the nine instruments onboard the satellite (`https://space.oscar.wmo.int/satellites/view/goes\_14`) and used in this study are available from the NOAA National Centers for Environmental Information (`https://ngdc.noaa.gov/stp/satellite/goes/dataaccess.html` and `https://satdat.ngdc.noaa.gov/sem/goes/data/avg`). The K-index data can be found here: `https://www.ngdc.noaa.gov/stp/GEOMAG/kp_ap.html` and the NOAA SEP data (flux at > 10 MeV) here: `https://umbra.nascom.nasa.gov/SEP/`. The files that include the algorithms used in this study can be found here: `https://github.com/skasapis/sdo_rad_belt`. The NIST ESTAR tables were accessed at `https://physics.nist.gov/PhysRefData/Star/Text/intro.html`.

Acknowledgments

We thank Mark Moldwin from the University of Michigan, Climate and Space Sciences and Engineering Department and the NASA Michigan Space Grant Consortium who partially funded Spiridon Kasapis' summer internship at NASA Goddard Space Flight Center. Juan Rodriguez was supported by NOAA cooperative agreement NA17OAR4320101. Barbara Thompson was supported by the NASA Internal Funding Science Model (ISFM) Center for HelioAnalytics Project. T. Paul O'Brien is acknowledged for his significant contribution and insightful comments on this work.

References

Berger, M., Inokuti, M., Anderson, H., Bichsel, H., & Dennis, J. (1984). Icru report 37: stopping powers for electrons and positrons. *J Int Comm Radiat Units Meas*, *19*(2).

Boyd, A. J., Spence, H., Reeves, G., Funsten, H., Skoug, R. M., Larsen, B. A., ... others (2021). Rbsp-ect combined pitch angle resolved electron flux data product. *Journal of Geophysical Research: Space Physics*, *126*(3), e2020JA028637.

Cai, L., Ma, S., Cai, H., Zhou, Y., & Liu, R. (2009). Prediction of SYM-H index by NARX neural network from IMF and solar wind data. *Science in China Series E: Technological Sciences*, *52*(10), 2877–2885.

Carlton, A., Pich, M. d. S.-S., Kim, W., Jun, I., & Cahoy, K. (2018). Using the galileo solid-state imaging instrument as a sensor of jovian energetic electrons. *IEEE Transactions on Nuclear Science*, *66*(1), 255–261.

Cliver, E. W. (2008). History of research on solar energetic particle (sep) events: the evolving paradigm. *Proceedings of the International Astronomical Union*, *4*(S257), 401–412.

Didkovsky, L., Judge, D., Jones, A., Rhodes Jr, E., & Gurman, J. (2006). Measuring proton energies and fluxes using eit (soho) ccd areas outside the solar disk images. *Astronomische Nachrichten: Astronomical Notes*, *327*(4), 314–320.

Fillius, R. W. (1968). Penetration of solar protons to four earth radii in the equatorial plane. In *Iaga comm. 5, solar-terrest. and cosmic-terrest. relationship conf.*

Hanser, F. (2011). Eps/hepad calibration and data handbook. *Assurance Technology Corporation, Carlisle, Mass*.

Kasapis, S., Zhao, L., Chen, Y., Wang, X., Bobra, M., & Gombosi, T. (2022). Interpretable machine learning to forecast sep events for solar cycle 23. *Space Weather*, *20*(2), e2021SW002842.

Kirk, M. S., Balasubramaniam, K., Jackiewicz, J., & Gilbert, H. R. (2017). The origin of sequential chromospheric brightenings. *Solar Physics*, *292*(6), 1–21.

Kirk, M. S., Balasubramaniam, K., Jackiewicz, J., & McAteer, R. J. (2014). Qualities of sequential chromospheric brightenings observed in hα and uv images. *The Astrophysical Journal*, *796*(2), 78.

Kress, B., Rodriguez, J., Mazur, J., & Engel, M. (2013). Modeling solar proton access to geostationary spacecraft with geomagnetic cutoffs. *Advances in Space Research*, *52*(11), 1939–1948.

Kurth, W., De Pascuale, S., Faden, J., Kletzing, C., Hospodarsky, G., Thaller, S., & Wygant, J. (2015). Electron densities inferred from plasma wave spectra obtained by the waves instrument on van allen probes. *Journal of Geophysical Research: Space Physics*, *120*(2), 904–914.

Lanzerotti, L. (1968). Penetration of solar protons and alphas to the geomagnetic equator. *Physical Review Letters*, *21*(13), 929.

Lanzerotti, L., Roberts, C., & Brown, W. (1967). Temporal variations in the electron flux at synchronous altitudes. *Journal of Geophysical Research*, *72*(23), 5893–5902.

Lario, D. (2005). Advances in modeling gradual solar energetic particle events. *Advances in Space Research*, *36*(12), 2279–2288.

Lemen, J. R., Akin, D. J., Boerner, P. F., Chou, C., Drake, J. F., Duncan, D. W., ... others (2011). The atmospheric imaging assembly (aia) on the solar dynamics observatory (sdo). In *The solar dynamics observatory* (pp. 17–40). Springer.

Lezniak, T., Arnoldy, R., Parks, G., & Winckler, J. (1968). Measurement and intensity of energetic electrons at the equator at 6.6 r e. *Radio Science*, *3*(7), 710–714.

Li, W., & Hudson, M. (2019). Earth's van allen radiation belts: From discovery to the van allen probes era. *Journal of Geophysical Research: Space Physics*, *124*(11), 8319–8351.

Li, X., Baker, D., Kanekal, S., Looper, M., & Temerin, M. (2001). Long term measurements of radiation belts by sampex and their variations. *Geophysical Research Letters*, *28*(20), 3827–3830.

Matthiä, D., Heber, B., Reitz, G., Meier, M., Sihver, L., Berger, T., & Herbst, K. (2009). Temporal and spatial evolution of the solar energetic particle event on 20 january 2005 and resulting radiation doses in aviation. *Journal of Geophysical Research: Space Physics*, *114*(A8).

Matzka, J., Stolle, C., Yamazaki, Y., Bronkalla, O., & Morschhauser, A. (2021). The geomagnetic kp index and derived indices of geomagnetic activity. *Space Weather*, *19*(5), e2020SW002641.

Menvielle, M., & Berthelier, A. (1991). The k-derived planetary indices: Description and availability. *Reviews of Geophysics*, *29*(3), 415–432.

Paulikas, G., & Blake, J. (1979). Effects of the solar wind on magnetospheric dynamics: Energetic electrons at the synchronous orbit. *Quantitative Modeling of Magnetospheric Processes, Geophys. Monogr. Ser*, *21*, 180–202.

Paulikas, G. A., & Blake, J. B. (1969). Penetration of solar protons to synchronous altitude. *Journal of Geophysical Research*, *74*(9), 2161–2168.

Pearson, K. (1896). Vii. mathematical contributions to the theory of evolution.—iii. regression, heredity, and panmixia. *Philosophical Transactions of the Royal Society of London. Series A, containing papers of a mathematical or physical character*(187), 253–318.

Pesnell, W. D., Thompson, B. J., & Chamberlin, P. (2011). The Solar Dynamics Observatory (SDO). In *The solar dynamics observatory* (pp. 3–15). Springer.

Rangarajan, G., & Lyemori, T. (1997). Time variations of geomagnetic activity indices kp and ap: an update. In *Annales geophysicae* (Vol. 15, pp. 1271–1290).

Reames, D. V. (2013). The two sources of solar energetic particles. *Space Science Reviews*, *175*(1), 53–92.

Rodriguez, J., Krosschell, J., & Green, J. (2014). Intercalibration of goes 8–15 solar proton detectors. *Space Weather*, *12*(1), 92–109.

Rodriguez, J., Onsager, T., & Mazur, J. (2010). The east-west effect in solar proton flux measurements in geostationary orbit: A new goes capability. *Geophysical Research Letters*, *37*(7).

Rowland, W., & Weigel, R. S. (2012). Intracalibration of particle detectors on a three-axis stabilized geostationary platform. *Space Weather*, *10*(11).

Scherrer, P. H., Schou, J., Bush, R., Kosovichev, A., Bogart, R., Hoeksema, J., ... others (2012). The helioseismic and magnetic imager (hmi) investigation for the solar dynamics observatory (sdo). *Solar Physics*, *275*(1), 207–227.

Sillanpää, I., Ganushkina, N. Y., Dubyagin, S., & Rodriguez, J. (2017). Electron fluxes at geostationary orbit from goes maged data. *Space Weather*, *15*(12), 1602–1614.

Spearman, C. (1961). *The proof and measurement of association between two things.* Appleton-Century-Crofts.

St Cyr, O., Kaiser, M., Meyer-Vernet, N., Howard, R., Harrison, R., Bale, S., ... others (2009). Stereo secchi and s/waves observations of spacecraft debris caused by micron-size interplanetary dust impacts. *Solar Physics*, *256*(1), 475–488.

Wanliss, J. A., & Showalter, K. M. (2006). High-resolution global storm index: Dst versus sym-h. *Journal of Geophysical Research: Space Physics*, *111*(A2).

Whitman, K., Egeland, R., Richardson, I. G., Allison, C., Quinn, P., Barzilla, J., ... others (2022). Review of solar energetic particle models. *Advances in Space Research*.

Woods, T., Eparvier, F., Hock, R., Jones, A., Woodraska, D., Judge, D., ... others (2010). Extreme Ultraviolet Variability Experiment (EVE) on the Solar Dynamics Observatory (SDO): Overview of science objectives, instrument design, data products, and model developments. *The solar dynamics observatory*, 115–143.

Young, P., Doschek, G., Warren, H., & Hara, H. (2013). Properties of a solar flare kernel observed by hinode and sdo. *The Astrophysical Journal*, *766*(2), 127.

Young, P., & Muglach, K. (2014). Solar dynamics observatory and hinode observations of a blowout jet in a coronal hole. *Solar Physics*, *289*(9), 3313–3329.

Young, P. R., Viall, N. M., Kirk, M. S., Mason, E. I., & Chitta, L. P. (2021). An analysis of spikes in atmospheric imaging assembly (aia) data. *Solar Physics*, *296*(12), 1–21.